NASA TECHNICAL MEMORANDUM

NASA TM X-62,278

NASA TM X-62,278

SURFACE MAGNETOMETER EXPERIMENTS: INTERNAL LUNAR PROPERTIES

Palmer Dyal, Curtis W. Parkin, and William D. Daily

Ames Research Center
Moffett Field, Calif. 94035
and
University of Santa Clara
Santa Clara, Calif. 94053

April 1973

Surface magnetometer experiments: Internal lunar properties

PALMER DYAL
NASA-Ames Research Center, Moffett Field, California 94035

CURTIS W. PARKIN
University of Santa Clara, Santa Clara, California 94053

WILLIAM D. DAILY
NASA-Ames Research Center, Moffett Field, California 94035

ABSTRACT

Magnetic fields have been measured on the lunar surface at the Apollo 12, 14, 15, and 16 landing sites. The remanent field values at these sites are respectively 38 γ, 103 γ (maximum), 3 γ, and 327 γ (maximum). Simultaneous magnetic field and solar plasma pressure measurements show that the remanent fields at the Apollo 12 and 16 sites are compressed and that the scale size of the Apollo 16 remanent field is $5 \leq L < 100$ km. The global eddy current fields, induced by magnetic step transients in the solar wind, have been analyzed to calculate an electrical conductivity profile. From nightside data it has been found that deeper than 170 km into the moon, the conductivity rises from 3×10^{-4} mhos/m to 10^{-2} mhos/m at 1000 km depth. Analysis of dayside transient data using a spherically symmetric two-layer model yields a homogenous conducting core of radius 0.9 R_{moon} and conductivity $\sigma = 10^{-3}$ mhos/m, surrounded by a nonconducting shell of thickness 0.1 R_{moon}. This result is in agreement with the conductivity profile determined from nightside data. The conductivity profile is used to calculate the temperature for an assumed lunar material of peridotite. In an outer layer ($\sim$ 170 km thick) the temperature rises to 850 - 1050 ^{o}K, after which it gradually increases to 1200 - 1500 ^{o}K at a depth of $\sim$ 1000 km. From lunar hysteresis curves it has been determined that the global relative magnetic permeability is $\mu/\mu_o = 1.029 \begin{smallmatrix} + 0.024 \\ - 0.019 \end{smallmatrix}$ for the whole moon. This permeability indicates that the moon responds as a paramagnetic or weakly ferromagnetic sphere; lunar iron abundance is calculated for various compositional models in a companion article (Parkin et al., 1973).

INTRODUCTION

Apollo astronauts have deployed five different magnetometers on the lunar surface which measure remanent and induced magnetic fields. Measurements from this network of instruments have been used to calculate the magnetic permeability, electrical conductivity, and temperature of the lunar interior. The fossil remanent magnetic field and its interaction with the solar wind plasma have been measured at three of the landing sites.

The fossil remanent field provides a record of the magnetic field environment that existed at the moon 3.7 to 4.2 billion years ago at the time the crustal material cooled below its Curie temperature. This fossil record indicates the possible existence of ancient large subsurface electrical currents, a solar or terrestrial field much stronger than exists at present, or to a lunar dynamo.

The remanent magnetic field is found to be compressed by the solar wind plasma. Properties of the compression are used to study the scale size and topology of the remanent field. The field also causes the solar wind ions and secondary lunar atmospheric ions to be deflected and therefore can be used to study gas accretion in the lunar regolith.

Analysis of the time dependence of eddy-current magnetic fields induced in the moon by solar field transients has yielded a continuous electrical conductivity profile of the lunar interior. The conductivity is related to internal temperature, which is calculated for assumed lunar material compositions.

Magnetic field measurements obtained when the moon is immersed in the steady geomagnetic tail field are used to calculate the magnetic permeability of the lunar interior. The permeability is related to the amount of permeable material and can be used to determine the abundance of iron in the moon.

EXPERIMENTAL TECHNIQUE

A network of magnetometers has been emplaced on the lunar surface by Apollo astronauts. The vector magnetic field is measured three times per second and transmitted to earth from each of the three sites shown in Fig. 1. Simultaneously magnetometers in lunar orbit, one on board the Explorer 35 (Sonett et al., 1967) and others on board Apollo subsatellites (Coleman et al., 1973) measure the ambient solar or terrestrial field and transmit this information to earth. Portable magnetometers have been used at the Apollo 14 and 16 sites, by the astronauts along their traverse, to measure remanent fields intrinsic to the moon.

Fig. 1

The external driving magnetic field in the lunar environment can vary considerably with the lunar orbital position (see Fig. 2). Average magnetic field conditions include relatively steady fields of magnitude $\sim 9\ \gamma$ ($1\ \gamma = 10^{-5}$ Gauss) in the geomagnetic tail, mildly turbulent fields averaging $\sim 5\ \gamma$ in the free-streaming solar plasma region, and turbulent fields averaging $\sim 8\ \gamma$ in the magnetosheath. Average solar wind velocity is ~ 400 km/sec in a direction approximately along the sun-earth line.

Fig. 2

Stationary lunar surface magnetometer (LSM)

The stationary magnetometer deployed at the Apollo 16 site in the Descartes region of the moon is shown in Fig. 3. Characteristics of this and similar instruments deployed at the Apollo 12 and 15 sites (Dyal et al., 1972) are given in Table I. A more detailed description of the stationary magnetometers is reported by Dyal et al. (1970).

Fig. 3

Table 1

Three orthogonal vector components of the magnetic field are measured by three fluxgate sensors located at the ends of 100-cm-long orthogonal booms. The sensors are separated from each other by 150 cm and are 75 cm above the ground. The instrument geometry, shown in Fig. 3, is such that each sensor is directed approximately 35° above the horizontal with the Z-sensor pointed toward the east, the X-sensor approximately toward the northwest, and Y-sensor completing a right hand orthogonal system. Orientation measurements with respect to lunar coordinates

are made with two devices. A shadowgraph is used by the astronaut to align and measure the azimuthal orientation with respect to the moon-to-sun line, and gravity level sensors measure tilt angles which are transmitted to earth. Long-term instrument stability is attained by extensive use of digital circuitry and by internally calibrating the analog portion of the instrument every 18 hours by command from earth. The analog output of the sensor is internally processed by a low-pass digital filter and a telemetry encoder, and the output is transmitted to earth via the central station S-band transmitter. The magnetometer has two data samplers, the analog-to-digital converter (26.5 samples/second) and the central station telemetry encoder (3.3 samples/second). The prealias filter following the sensor electronics has attenuations of 3db at 1.7 Hz and 58 db at the Nyquist frequency (13.2 Hz), with an attenuation rate of 22 db/octave. The four-pole Bessel digital filter has an attenuation of 3 db at 0.3 Hz and 48 db at the telemetry sampling Nyquist frequency (1.6 Hz).

The instrument can also be used as a gradiometer by sending commands to operate three motors in the instrument which rotate the sensors such that all simultaneously align parallel first to one of the boom axes, then to each of the other two boom axes in turn. This alignment capability permits the vector gradient in the plane of the sensors to be calculated and also permits an independent measurement of the magnetic field vector at each sensor position.

Lunar portable magnetometer (LPM)

The portable magnetometer developed for the Apollo 16 mission to Descartes is shown in Fig. 3(b) and the instrument characteristics are given in Table 1. A more detailed description of the instrument is reported by Dyal et al. (1973).

The LPM instrument was designed to be a totally self-contained, portable experiment package. Three orthogonally oriented fluxgate sensors are mounted on the top of a tripod, positioned 75 cm above the lunar surface. These sensors are connected by a 15-meter-long cable to an electronics box (mounted on the lunar roving vehicle), which contains a battery, electronics and three digital displays used to read the field output.

Lunar orbiting magnetometers

The ambient steady-state and time-dependent magnetic fields in the lunar environment are measured by the Explorer 35 satellite magnetometer. The satellite, launched in July 1967, has an orbital period of 11.5 hours, aposelene of 9390 km, and periselene of 2570 km (see Fig. 2 insert). The Explorer 35 magnetometer measures three magnetic field vector components every 6.14 sec at 0.4 γ resolution; the instrument has an alias filter with 18 db attenuation at the Nyquist frequency (0.08 Hz) of the spacecraft data sampling system. A more detailed description of the instrument is reported by Sonett et al. (1967).

The Apollo 15 and 16 subsatellite magnetometers, orbiting approximately 100 km above the lunar surface, have also measured fields intrinsic to the moon. These instruments are described by Coleman et al. (1973).

REMANENT MAGNETIC FIELD MEASUREMENTS

Remanent magnetic fields have been measured at the Apollo 12, 14, 15, and 16 landing sites on the lunar surface. At the Apollo 14 Fra Mauro and 16 Descartes sites, portable magnetometers were used by the astronauts to measure the remanent fields at different locations along their traverses. The measured fields and their locations are listed in Table 2. Results show that magnetic fields are lower in the mare regions (3 to 100 gammas) than in the Descartes highland region (112 to 327 gammas). The field magnitude gradients vary from 1.2 gammas/kilometer to 370 gammas/kilometer at different locations on the moon.

Table 2

The source for the measured permanent magnetic field on the lunar surface is generally considered to be the remanence in the near-surface material. Remanent magnetism has been measured in returned lunar samples by many investigators (e.g. Strangway et al., 1973; Nagata, 1972; Runcorn et al., 1970). Also, the Apollo 15 and 16 subsatellite magnetometers have directly measured the lunar remanent fields from orbit and found larger fields associated with the highlands than with the mare regions (Coleman et al., 1973).

Measured remanent field values are much smaller at the subsatellite altitude (1 γ at 100 km) than at the surface (300 γ at Descartes); since the field magnitudes fall off rapidly with distance, the sources must be small in extent and probably are confined to the near-surface crustal materials. The lack of a measurable whole-moon dipolar magnetic field (Russell et al., 1973) is another indication that the crust is the only portion of the moon that is magnetized.

The magnetic fields measured at five different locations at the Descartes landing site are the largest extraterrestrial fields yet measured in situ. The largest distance between measurements was 7.1 kilometers. A schematic representation of the measured field vectors is shown in Fig. 4. All vectors point downward except the one at Site 5 near Stone Mountain, which points upward. This suggests that the material underlying Stone Mountain has undergone different geological processes than that underlying the Cayley Plains and North Ray Crater.

Fig. 4

Lunar sample measurements and field measurements by orbiting surface instruments all indicate that the moon is covered with remanent magnetic field sources which show a strong regional variation. The lunar crustal material probably was magnetized as it cooled below the Curie temperature in the presence of a strong ambient magnetic field about 4 billion years ago (Gopulan et al., 1971). Sources of this ancient ambient field which no longer exists at the moon, include an extinct lunar dynamo, a stronger solar or terrestrial field, and a field of thermoelectric origin. This latter field could have been generated during the mare basin flooding era.

It has been determined that the thermoremanent magnetization of lunar samples has resulted from their cooling below the Curie point in a field of a few thousand gammas (Gose et al., 1973; Pearce et al., 1973). We have initiated an investigation of thermoelectrically driven currents to account for these fields. Thermoelectric potential is a function of the thermal gradient and electrical properties of the geological material. We model a mare basin as a cylinder which has an axial temperature gradient.

Thermal gradients in the cooling mare lava could produce a Thomson thermoelectromotive force which would drive currents axially through the mare cylinder. The solar wind plasma, highly conducting along magnetic field lines, could provide a return path to complete the electrical circuit from the top surface of the lava to the lunar surface outside the mare and back into the mare through the lunar interior.

The upper limit of the field generated at the mare edge by this process is $B = \mu_o E \sigma R(\Delta T)/2L$ where R and L are the cylinder radius and length, σ is the electrical conductivity, E is the thermoelectromotive force and ΔT is the temperature difference across the cylinder. Telkes (1950) reports maximum thermoelectromotive force magnitudes of the order of 10^2 μ V/deg. in geological materials. At the edge of a disk of $R/L = 10^3$, $\Delta T = 10^3$ ^oK, $\sigma_{mean} = 10^{-1}$ mhos/m, and $E = 10^2$ μ V/deg., fields of several thousand gammas are possible. Such fields near a mare disk would produce thermoremanent magnetization in the moon of magnitudes measured in lunar samples.

REMANENT MAGNETIC FIELD INTERACTION WITH THE SOLAR WIND

Interaction of the solar wind with the remanent magnetic field has been measured at the Apollo 12 and 16 landing sites. The solar plasma is directly measured at the Apollo 12 and 15 sites (Clay et al., 1972) and simultaneous measurements of the magnetic field at the Apollo 12 and 16 sites show a compression of the steady field as a function of the solar wind pressure. This is schematically shown in the Fig. 5 insert. Time-dependent induction fields are negligible for one-hour averages of LSM field measurements, and the dominant fields measured at the surface (Dyal and Parkin, 1973) are $\underline{B}_A = \underline{B}_E + \underline{B}_R + \underline{\Delta B}$. In this equation $\underline{B}_A$ is the total magnetic field measured on the lunar surface by an Apollo magnetometer, $\underline{B}_E$ is the extralunar field measured by the orbiting Explorer 35 magnetometer, $\underline{B}_R$ is the unperturbed remanent field local to the site (measured when the moon is shielded from the solar wind in the earth's magnetotail), and ΔB is the change in the

remanent field due to its interaction with the solar wind plasma. One-hour average plots in Fig. 5 show that the change in remanent field pressure $\Delta B^2/8\pi$ is related to the plasma pressure nmv^2 (n is proton density, m is proton mass, and v is plasma bulk speed).

The nature of the correlation between magnetic field and plasma pressures is further illustrated in Fig. 6, which shows data from several lunations at the Fig. 6 Apollo

12 and 16 LSM sites. The pressures are related throughout the measurement range. The magnitudes of magnetic pressure changes at the Apollo 12 and 16 LSM sites are in proportion to their unperturbed steady field magnitudes of 38 γ and 235 γ, respectively.

Properties of the remanent field interaction with the solar wind can be used to estimate the scale size of the remanent field (Barnes et al., 1971). The Apollo 12 scale size L has previously been calculated to be 2km $< L <$ 200 km (Dyal et al., 1972). For the Apollo 16 field, portable magnetometer measurements over the lunar roving vehicle traverse showed that $L \geq 5$ km; the Apollo 16 subsatellite magnetometer showed no field attributable to the Descartes area at orbital altitude, implying that $L <$ 100 km. Therefore, the Apollo 16 remanent field scale size is $5 \leq L <$ 100 km.

Previous experimental limits (Dyal and Parkin, 1971) of the lunar unipolar induction fields have been supplemented with a more extensive statistical analysis of Explorer 35 and Apollo 12 and 15 LSM magnetometer data to show that the toroidal mode induction fields at the lunar surface are less than a few gammas. The results of this study confirm the idea that the lunar crust is of sufficient electrical resistivity and thickness to quench current flow from unipolar induction.

GLOBAL EDDY CURRENT INDUCTION: ELECTRICAL CONDUCTIVITY AND TEMPERATURE

Electrical conductivity and temperature of the moon are calculated from global eddy current response to magnetic field transients in the solar wind. When a magnetic discontinuity in the interplanetary magnetic field passes the moon, an eddy current field is induced in the moon which opposes the change in the external field (see Fig. 7). The induced field thereafter decays with a time dependence which is a function of the electrical conductivity distribution in the lunar interior. Simultaneous measurements of the transient driving field (by Explorer 35) and the lunar response field (by an Apollo surface magnetometer) allow calculation of the lunar conductivity. Since conductivity is related to

Fig. 7

temperature, a temperature profile can be calculated for an assumed compositional model of the lunar interior.

Lunar eddy current fields form an induced lunar magnetosphere which is distorted in a complex manner due to flow of solar wind plasma past the moon, as illustrated in Fig. 7. The eddy current field is compressed on the dayside of the moon and is swept downstream and confined to the "cavity" on the lunar nightside. Because of the complexity earliest models included a theory for transient response of a sphere in a vacuum, to model lunar response as measured on the lunar nightside (Dyal and Parkin, 1971), and a harmonic theory of a moon totally confined by the solar wind to model response as measured on the lunar dayside (Sonett et al., 1971). Both harmonic and transient approaches have subsequently been further developed. Transient analysis has evolved to include a continuous conductivity profile (Dyal et al., 1972), and more recently has included effects of cavity confinement on the nightside radial data (Dyal and Parkin, 1973). In this paper we extend the evolutionary process to include effects of cavity confinement on nightside tangential data and to introduce analysis of magnetic step transients measured on the lunar dayside. We find that these additional calculations yield conductivity profiles which are consistent with our earlier results.

1. Lunar Nightside Data Analysis

Fig. 8 shows simultaneous measurements of a step transient by the lunar orbiting Explorer 35 magnetometer and the Apollo 12 LSM located on the lunar nightside. The Apollo data qualitatively show response of a sphere in a vacuum: damping in the radial (B_{Ax}) component and overshoot in tangential components ($B_{Ay,z}$). Averages of normalized decay curves of radial data have been analyzed (Dyal and Parkin, 1973) to yield the conductivity profile illustrated in Fig. 9(a); the corresponding temperature profiles for two assumed lunar compositional models are shown in Fig. 9 (b).

Fig. 8

Fig. 9

2. Lunar Dayside Data Analysis

Fig. 10 shows an example of a transient measured by the Apollo 12 LSM on the lunar dayside. Comparison with Fig. 8 shows these qualitative differences between dayside and nightside transient data: (1) Apollo dayside radial response is not damped, as is the nightside response, but tends to track the Explorer 35 radial-component measurements, and (2) the overshoot in tangential y and z components is much greater in dayside data, illustrating solar wind compression of the eddy current field on the dayside. Theoretical solutions for an eddy current field totally confined to a sphere of homogeneous conductivity σ and permeability μ are derived from Maxwell's equations in the Appendix. For the case of an external magnetic step transient of magnitude $|\underline{\Delta B}_E|$, applied to the lunar sphere at time t=0, the solutions for the components of the vector field measured on the lunar dayside are expressed as follows:

$$B_{Ax} = B_{Ex} \tag{1}$$

$$B_{Ay,z} = B_{Ey,z} + \Delta B_{Ey,z} \left[\frac{3\lambda^3}{2(1-\lambda^3)} \right] F(t) \tag{2}$$

$$\text{where } F(t) = \frac{6}{1-\lambda^3} \sum_s \exp\left[-z_s^2\, t/\mu\,\sigma\, R_c^2\right] \Big/ \left[z_s^2 + \left((h-\tfrac{1}{2})^2 - \tfrac{9}{4} \right) \right] \tag{3}$$

In the above equations $\lambda = R_c/R_m$, R_c = radius of conducting core (surrounded by a nonconducting outer shell of thickness $R_m - R_c$); and z_s is a solution of the characteristic equation $\tan z_s = z_s(h-2)/(z_s^2 + (h-2))$. The components of B_A are expressed in the ALSEP coordinate system which has its origin on the lunar surface at a magnetometer site. The x-axis is directed radially outward from the lunar surface; the y and z axes are tangential to the surface, directed eastward and northward respectively. Equation (1) shows that for this homogeneous-core theory the surface field radial component B_{Ax} tracks the external radial component B_{Ex}; equation (2) illustrates that tangential components will overshoot a step input field with an amplification factor which is a function of the conducting core radius R_c, after which the eddy current field will decay as a function

of time, μ, σ, and R_c. Fig. 11 shows averages of normalized lunar dayside tangential components in response to seven transient events (error bars are standard deviations). Apollo data have been normalized by dividing by the Explorer 35 step magnitudes to give the response to an effective unit step driving field. The overshoot maximum is amplified by a factor of 5 by solar wind dayside compression. In this homogeneous theory, this amplification factor is used with equation (2) to calculate $\lambda = R_c/R_m = 0.9$. Superimposed on the figure is a family of curves varying with conductivity σ ($\mu = \mu_o$, the permeability of free space). The data show a good fit to a lunar model with a homogeneous core of radius $R_c = 0.9\ R_m$ and conductivity $\sigma \sim 10^{-3}$ mhos/m. Fig. 9 shows this homogeneous conductivity profile superimposed on the continuous conductivity profile calculated from nightside radial magnetic field data; the dayside calculation fits within the error bars of the nightside calculation to depths allowed by the time duration of the events in Fig. 11.

Fig. 11

3. Asymmetric confinement of the lunar induced magnetosphere

Having considered spherically symmetric models to treat nightside and dayside data, we now proceed to the case of asymmetric confinement of the lunar magnetosphere, illustrated in Fig. 7. Previous theoretical treatments of this problem include a two-dimensional time-dependent approach (Reitz et al., 1972) and a three-dimensional quasi-static approach (Schubert et al., 1973). At the time of this writing, a complete time-dependent solution for the lunar magnetosphere has not been developed; therefore our present approach is to show general consistency of daytime and nighttime transient response data with theoretical approximations presently available.

First we model the effects of partial confinement by considering the case of a point dipole confined by a capped cylindrical superconductor (Dyal and Parkin, 1973). Fig. 12 shows the theoretical solution for amplification of tangential (transverse) components due to asymmetric confinement of the dipole field by the

Fig. 12

superconductor. This models the asymmetric solar wind confinement of an induced dipole in the moon. Data points shown in Fig. 12 are laboratory measurements made by placing a small samarium-cobalt magnet inside a helium-cooled superconducting cylinder; data are seen to be in agreement with theory.

This asymmetric confinement yields the value of the overshoot of the tangential eddy current field at the lunar surface antisolar point. At $r/R = 1$ in

Fig. 12, analogous to the location of the lunar surface antisolar point, the theoretical confined-to-unconfined ratio is 1.5. In the previous section we found that dayside transient data fit a lunar model with conducting core radius $R_c=0.9R_m$. In unconfined vacuum theory for $R_c/R_m=0.9$, the tangential component overshoot is $1 + \frac{1}{2}(R_c/R_m)^3 = 1.36$. Multiplying by the confined-to-unconfined ratio of 1.5, we find that for the asymmetric case, the initial overshoot of normalized data measured at the antisolar point should be 2.0. We have averaged tangential events all obtained within 6^o of the antisolar point and have calculated an overshoot of 2.0 ± 0.3, showing agreement with the confined-dipole theory and laboratory data.

A final check on the overshoot magnitude for the confined case is obtained by comparison with the "quasi-static" theoretical solutions of Schubert et al. (1973). This theory considers the response of an infinitely conducting, spherical core confined inside a hemispherically capped cylinder, also of infinite conductivity. The response of the infinitely conducting core is the same as that of our model with a core of finite conductivity, at the instant the external field transient occurs. Fig. 5 of Schubert et al. (1973) gives the overshoot to be ~ 1.9 for the case $R_c/R_m=0.9$. This value is well within our nightside data overshoot limits of 2.0 ± 0.3.

In conclusion, we have shown that our earlier electrical conductivity profile (Fig. 9), calculated using radial components of nightside data, is still consistent with more recent calculations which consider effects of solar wind confinement on both dayside and nightside magnetic fields. Further refinement of the conductivity profile of Fig. 9 must await the development of a time-dependent asymmetric theory.

MAGNETIZATION INDUCTION AND GLOBAL MAGNETIC PERMEABILITY

When the moon is in a quiet region of the geomagnetic tail, solar wind interaction fields and the induced eddy current lunar field are negligible (Parkin et al., 1973), and the total field at the lunar surface is $\underline{B}_A = \underline{B}_E + \underline{B}_\mu$.

The magnetic moment $\underline{m}_{\mu}$ of the magnetization field $\underline{B}_{\mu}$ is proportional to the external field $\underline{B}_E$; that is, $\underline{m}_{\mu} = C\,\underline{B}_E$. (The proportionality constant C in turn depends on the permeability and the dimensions of the permeable region of the Moon.) The magnetization of the lunar sphere by the terrestrial magnetic field is shown schematically in Fig. 13.

For the case of a homogeneous permeable lunar sphere of relative permeability μ, the ALSEP components of the total surface magnetic field (Jackson, 1962) are:

$$B_{Ax} = (1+2F)\,B_{Ex} \qquad (4)$$

$$B_{Ay,z} = (1-F)\,B_{Ey,z} \qquad (5)$$

$$\text{where } F = \frac{\mu-1}{\mu+2} \qquad (6)$$

A plot of B_{Ax} vs. B_{Ex} is in effect a plot of a B-H hysteresis curve. For cases where the ratio B_{Ax}/B_{Ex} is a constant, i.e., for low field B_{Ex}, the hysteresis curve should take the form of a straight line. Fig. 14 shows a plot of radial components of Apollo 12 surface field (B_{Ax}) versus the geomagnetic tail field (B_{Ex}) measured by Explorer 35. A least-squares fit and slope calculation determine the factor $F = 0.0095 \pm 0.0060$, which is used in equation (6) to determine the bulk relative magnetic permeability of the moon: $\mu = 1.029 \pm \begin{matrix} 0.024 \\ 0.019 \end{matrix}$.

The relative permeability is greater than 1.0 for both extremes of the error limits, indicating that when immersed in a uniform, steady geomagnetic tail field, the moon is magnetized along the direction of the tail field, causing the moon as a whole to have the properties of a magnetized paramagnetic or weakly ferromagnetic sphere. Iron abundance in the moon is also estimated from lunar hysteresis curves, using various compositional models of the lunar interior. These results are reported in a companion article in this volume (Parkin et al., 1973).

SUMMARY

1. Remanent magnetic field measurements

The remanent magnetic fields measured on the lunar surface are 38 γ at Apollo 12 in Oceanus Procellarum; 103 γ and 43 γ at two Apollo 14 sites separated by 1.1 km in Fra Mauro; 3.4 γ at the Apollo 15 Hadley Rille site; and 189 γ, 112 γ, 327 γ, 113 γ, and 235 γ at five Apollo 16 sites in the Descartes region, over a distance of 7.1 km. Simultaneous measurements by a lunar orbiting subsatellite and the Apollo surface magnetometers, and remanence in the returned samples, have shown that the near-surface crustal material is magnetized over most of the lunar globe. The field sources which show a strong regional variation over much of the moon, were probably magnetized as the crustal material cooled below the Curie temperature in the presence of a strong ambient magnetic field about 4 billion years ago. A possible source of this ancient ambient field is thermoelectric currents generated during mare basin flooding.

2. Remanent magnetic field interaction with the solar wind

Measurements show that the remanent fields at the Apollo 12 and 16 sites are compressed by the solar wind. The 235 γ remanent field at the Apollo LSM site is compressed to 265 γ by a solar wind pressure increase of 1.5×10^{-7} dynes/cm^2. The scale size L of the Apollo 16 remanent field has been determined to be in the range 5 km $\leq$ L < 100 km. The 5 km lower limit is calculated from measurements of the field-plasma interaction, and the 100 km upper limit is deduced from lunar orbiting subsatellite measurements.

3. Global eddy current induction: Electrical conductivity and temperature

The electrical conductivity and temperature of the moon are calculated from global eddy current response to magnetic field transients in the solar wind. Using a spherically symmetric model, a continuous conductivity profile, with error limits, has been determined from radial step transient response data. Dayside

transient response data, compared to the theoretical response of a totally confined sphere, yields a homogeneous conductivity profile ($\sigma \sim 10^{-3}$ for a core of $R_c/R_m = 0.9$) which lies within the error limits of the nightside radial results.

Nightside response is adjusted to account for asymmetric confinement of eddy current fields by two methods: using laboratory data obtained by confining a dipole field within a superconducting cylinder, and using a quasistatic theory for confinement of eddy current fields of a spherical source. Initial overshoots of nightside tangential data agree within experimental error with laboratory and theoretical results. An upper limit on the unipolar induction field has been determined which shows that the outer crustal layer, ~170 km thick, is a relatively poor electrical conductor compared to the underlying material. Deeper than 170 km, the conductivity rises from 3×10^{-4} mhos/meter to 10^{-2} mhos/m at 1000 km depth. These conductivities are used to calculate temperatures for a lunar model composed of peridotite and show an outer layer, ~ 170 km thick, in which the temperature rises from 250°K to 850-1050°K, then a gradual increase to 1200-1500°K at a depth of ~ 1000 km.

4. Magnetization induction and global magnetic permeability

Magnetic hysteresis curves have been measured for the moon by simultaneous data obtained from the orbiting Explorer 35 and surface Apollo 12 and 15 magnetometers. From these curves the bulk relative magnetic permeability of the moon is determined to be $\mu = 1.029 \begin{smallmatrix} + 0.024 \\ - 0.019 \end{smallmatrix}$. This permeability indicates that the moon is a paramagnetic or weakly ferromagnetic sphere and the iron abundance is estimated for various compositional models in a companion article (Parkin et al., 1973).

ACKNOWLEDGEMENTS

We thank Drs. C. W. Snyder and D. R. Clay of the Jet Propulsion Laboratory for use of solar wind spectrometer data and Drs. C. P. Sonett and D. S. Colburn of NASA-Ames Research Center for use of Explorer 35 data. We have especially appreciated working with Dr. T. J. Mucha of Computer Sciences Corporation in the analysis of dayside magnetic transients. We also acknowledge the efforts of Messrs. J. Keeler and C. Privette for experiment fabrication and testing, and K. Lewis and M. Legg and their team members for help in computer programming and data reduction.

REFERENCES

Barnes A., Cassen P., Mihalov J.D., and Eviat A. (1971) Permanent lunar surface magnetism and its deflection of the solar wind. Science 171, 716-718.

Clay D.R., Goldstein B.E., Neugebauer M., and Snyder C.W. (1973) Solar-wind spectrometer experiment. In Apollo 15 Preliminary Science Report, NASA SP-289, pp. 10-1 to 10-7.

Colburn D.S., Currie R.G., Mihalov J.D., and Sonett C.P. (1967) Diamagnetic solar-wind cavity discovered behind the moon, Science 168, 1040-1042.

Coleman P.J. Jr., Lichtenstein B.R., Russell C.T., Schubert G., and Sharp L.R. (1973) The particles and fields subsatellite magnetometer experiment. In Apollo 16 Preliminary Science Report, NASA SP-315, pp. 23-1 to 23-13.

Dyal P. and Parkin C.W. (1971) The Apollo 12 magnetometer experiment: internal lunar properties from transient and steady magnetic field measurements. "Proc. Second Lunar Sci. Conf. Geochim. Cosmochim. Acta" Suppl. 2, Vol. 3, pp. 2391-2413. MIT Press.

Dyal P. and Parkin C.W. (1973) Global electromagnetic induction in the moon and planets. Phys. Earth Planet. Interiors (in press).

Dyal P., Parkin C.W., and Sonett C.P. (1970) Lunar surface magnetometer. IEEE Trans. on Geoscience Electronics GE-8 4, 203-215.

Dyal P., Parkin C.W., and Cassen P. (1972) Surface magnetometer experiments: Internal lunar properties and lunar surface interactions with the solar plasma. "Proc. Third Lunar Sci. Conf. Geochim. Cosmochim. Acta" Suppl. 3, vol. 3, pp. 2287-2307. MIT Press.

Dyal P., Parkin C.W., Sonett C.P., DuBois R.L., and Simmons G. (1973) Lunar portable magnetometer experiment. In Apollo 16 Preliminary Science Report, NASA SP-315, pp. 12-1 to 12-8.

Gopulan K., Kaushal S., Lee-Hu, C., and Wetherill G.W. (1970) Rb-Sr and U, Th-Pb ages of lunar materials. "Proc. Apollo 11 Lunar Sci. Conf. Geochim. Cosmochim. Acta" Suppl. 1, Vol. 2, pp. 1195-1205. Pergamon Press.

Gose W.A., Strangway D.W., and Pearce G.W. (1973) A determination of the intensity of the ancient lunar magnetic field. The Moon (in press).

Jackson J.D. (1962) Classical Electrodynamics. John Wiley and Sons.

Nagata T., Fisher R.M., Schwerer F.C., Fuller M.D., and Dunn J.R. (1972) Rock magnetism of Apollo 14 and 15 materials. "Proc. Third Lunar Sci. Conf. Geochim. Cosmochim. Acta" Suppl. 3, Vol. 3, pp. 2423-2447. M.I.T. Press.

Parkin C.W., Dyal P., and Daily W.D. (1973) Iron abundance in the moon from magnetometer measurements. Submitted to "Proc. Fourth Lunar Sci. Conf., Geochim. Cosmochim. Acta" Suppl. 4, Vol. 3.

Pearce G.W., Strangway D.W., and Gose W.A. (1972) Remanent magnetization of the lunar surface. "Proc. Third Lunar Sci. Conf. Geochim. Cosmochim. Acta" Suppl. 3, Vol. 3, pp. 2449-2464. MIT Press.

Reitz A.C., Paul D.L., and Madden T.R. (1972) The effects of boundary condition asymmetries on the interplanetary magnetic field-moon interaction. The Moon 4, 134-140.

Runcorn S.K., Collinson D.W., O'Reilly W.O., Battey M.H., Stephenson A., Jones J.M., Manson A.J., and Readman P.W. (1970) Magnetic properties of Apollo 11 lunar samples. "Proc. Apollo 11 Lunar Sci. Conf. Geochim. Cosmochim. Acta" Suppl. 1, Vol. 3, pp. 2369-2387. Pergamon Press.

Russell C.T., Coleman P.J., Lichtenstein B.R., Schubert G., and Sharp L.R. (1973) Apollo 15 and 16 subsatellite measurements of the lunar magnetic field (abstract). "In Lunar Science - IV" (editors J.W. Chamberlain and C. Watkins) pp. 645-646, Lunar Science Institute, Houston.

Schubert G., Sonett C.P., Schwartz K., and Lee H.J. (1973) The induced magnetosphere of the moon I. Theory. Submitted to Rev. Geophys. Space Phys.

Sharp L.R., Coleman P.J., Lichtenstein B.R., Russell C.T., and Schubert G. (1972) Orbital mapping of the lunar magnetic field. Institute of Geophysics and Planetary Physics, UCLA Publication No. 1092-13.

Sonett C.P., Colburn D.S., Currie R.G., and Mihalov J.D. (1967) The geomagnetic tail; topology, reconnection, and interaction with the moon. In Physics of the Magnetosphere (editors R.L. Carovillano, J.F. McClay, and H.R. Radoski). D. Reidel.

Sonett C.P., Schubert G., Smith B.F., Schwartz K., and Colburn D.S. (1971) Lunar electrical conductivity from Apollo 12 magnetometer measurements: Compositional and thermal inferences. "Proc. Second Lunar Sci. Conf. Geochim. Cosmochim. Acta" Suppl. 2, Vol. 3, pp. 2415-2431. MIT Press.

Strangway D.W., Gose W.A., Pearce G.W., and Carnes J.G. (1973) Magnetism and the history of the moon. Proc. of the 18th Annual Conf. on Magnetism and Magnetic Materials, J. Applied Phys. (in press).

Telkes M. (1950) Thermoelectric power and electrical resistivity of minerals. Am. Mineralogist 35, No. 7.

APPENDIX

We consider a sphere which has a conducting core of radius R_c and electrical conductivity σ, with an insulating crust of thickness $R_m - R_c$, imbedded in a uniform magnetic field $\underline{B}_E$. Magnetic permeability everywhere is that of free space, μ_o. At time $t=0$ the field is terminated such that $b(t) = 1$ for $t \leq 0$; $b(t)=0$ otherwise. If the induced fields are confined within the radius R_m, azimuthal symmetry and continuity of the radial field across the boundary allow the magnetic vector potential to be written

$$\underline{A} = \begin{cases} \underline{\Phi} \sin\theta \; U(r,t) & r < R_c \\ \underline{\Phi} \sin\theta \; V(r,t) & R_c < r < R_m \end{cases} \tag{1}$$

which must satisfy the Helmholtz equation $\nabla^2 \underline{A} = \mu \sigma \dfrac{\partial \underline{A}}{\partial t}$.

The boundary conditions on the radial component of field requires

$$\frac{1}{r\sin\theta} \frac{\partial}{\partial\theta} (\sin\theta \, \underline{A}) \Big|_{r=R_m} = \underline{\Phi} \, \Delta B_E b(t) \cos\theta \, . \tag{2}$$

Equations (1) and (2) yield the differential equations

$$r^{-2} \left[r^2 U_{rr} + 2rU_r - 2U \right] = \mu_o \sigma U_t \tag{3}$$

$$U(0,t) \text{ is bounded}$$

where the r subscript denotes $\partial/\partial r$, and

$$\begin{aligned} r^2 V_{rr} + 2rV_r - 2V &= 0 \\ V(R_m,t) &= 0 \end{aligned} \tag{4}$$

with the conditions

$$U(R_c,t) + R_c U_r(R_c,t) = V(R_c,t) + R_c V_r(R_c,t)$$

$$U(R_c,t) = V(R_c,t).$$

It can be verified that the bounded solution to equation (3) is

$$U(r,t) = \sum_s a_s j_1(k_s r) \exp\left(- \frac{k_s^2}{\mu_o \sigma} t \right) \tag{5}$$

and the time-decay solution to equation (4) is

$$V(r,t) = \left(r - \frac{R_m^3}{r^2}\right)\sum_n A_n \exp(-q_n t) \quad . \qquad (6)$$

For the boundary conditions to hold at all times we must have

$$q_n = \frac{k_s^2}{\mu_o \sigma} = \frac{z_s^2}{\pi^2 T} \; ; \; s = n = 1,2,3, \ldots .$$

where $z_s = k_s R_c$, $T = R_c^2 \mu_o \sigma / \pi^2$ with the coefficients A_n and $a_n (s=n)$ defined by $a_s \left[z_s j_1'(z_s) + j_1(z_s)\right] = A_s \frac{R_m}{\lambda^2}(2\lambda^3 + 1)$; $\lambda = R_c/R_m$

and $a_s j_1(z_s) = A_s \frac{R_m}{\lambda^2}(\lambda^3 - 1)$

which in turn determine the characteristic equation for z_s. After elimination of the unknown constants a_s, and A_s, the characteristic equation is

$$z_s j_1'(z_s) + h j_1(z_s) = 0$$

Then the eigenvalue z_s is a solution of

$$\tan z_s = \frac{(h-2) z_s}{z_s^2 + (h-2)} \qquad (7)$$

where

$$h = \frac{2 + \lambda^3}{1 - \lambda^3}$$

The initial condition $U(r,0) = \Delta B_E r/2$ applied to equation (5) requires

$$a_s = \frac{\Delta B_E R_c (1+h)}{\left[z_s^2 + (h-2)(h+1)\right] j_1(z_s)}$$

which in turn defines

$$A_s = - \frac{\Delta B_E \lambda^3 (1+h)}{(1-\lambda^3)\left[z_s^2 + (h-2)(h+1)\right]} .$$

The vector potential can now be written

$$\underline{A} = -\underline{\Phi} \frac{\Delta B_E \sin\theta}{2} \left(\frac{\lambda^3}{1-\lambda^3}\right)\left(r - \frac{R_m^3}{r^2}\right) F(t) \qquad R_c \leq r \leq R_m \qquad (8)$$

where z_s are the nontrivial roots of equation (7) and

$$F(t) = \frac{6}{1-\lambda^3} \sum_s \left[z_s^2 + (h-2)(h+1)\right]^{-1} \exp\left(-z_s^2 t/\pi^2 T\right)$$

The induced eddy current field in the outer shell is given by the curl of equation (8):

$$B_r(r,\theta,t) = - \Delta B_E \cos\theta \left(\frac{\lambda^3}{1-\lambda^3}\right)\left[1 - \left(\frac{R_m}{r}\right)^3\right] F(t)$$

$$B_\theta(r,\theta,t) = \Delta B_E \sin\theta \left(\frac{\lambda^3}{1-\lambda^3}\right)\left[1 + \tfrac{1}{2}\left(\frac{R_m}{r}\right)^3\right] F(t)$$

We rotate the (r, θ, Φ) coordinate system about $\hat{r}$ to coincide with the ALSEP (x, y, z) system (defined in text) and evaluate the fields at $r=R_m$ to get the time-dependent solutions:

$$B_{Ax}(t) = B_{Ex}(t)$$

$$B_{Ay,z}(t) = B_{Ey,z}(t) + \Delta B_{Ey,z}\left[\frac{3}{2}\left(\frac{\lambda^3}{1-\lambda^3}\right)\right] F(t) .$$

Table 1.

Apollo Surface magnetometer characteristics.

Parameter	Apollo 16 stationary magnetometer (LSM)	Apollo 16 portable magnetometer(LPM)
Ranges, gammas (each sensor)	0 to ± 200 0 to ± 100 0 to ± 50	0 to ± 256
Resolution, gammas	0.1	1.0
Frequency response, Hz	dc to 3	dc to 0.05
Angular response	Cosine of angle between field and sensor	Cosine of angle between field and sensor
Sensor geometry	3 orthogonal sensors at ends of 100 cm booms	3 orthogonal sensors in 6 cm cube
Analog zero determination	180° flip of sensor	180° flip of sensor
Power, watts	3.5	1.5 (battery)
Weight, kg	8.9	4.6
Size, cm	63 x 28 x 25	56 x 15 x 14
Operating temperature °C	-50 to +85	0 to +50
Commands	10 ground: 1 spacecraft	—

Table 2. Summary of Lunar Surface Remanent Magnetic Field Measurements.

Site	Coordinates, deg.	Field Magnitude, Gammas	Magnetic-field components, gammas		
			Up	East	North
Apollo 16:					
ALSEP Site	8.9°S, 15.5°E	235 ± 4	-186 ± 4	-48 ± 3	+135 ± 3
Site 2		189 ± 5	-189 ± 5	+3 ± 6	+10 ± 3
Site 5		112 ± 5	+104 ± 5	-5 ± 4	-40 ± 3
Site 13		327 ± 7	-159 ± 6	-190 ± 8	-214 ± 6
LRV Final Site		113 ± 4	-66 ± 4	-76 ± 4	+52 ± 2
Apollo 15:					
ALSEP Site	26.1°N, 3.7°E	3.4 ± 2.9	+3.3 ± 1.5	+0.9 ± 2.0	-0.2 ± 1.5
Apollo 14:	3.7°S, 17.5°W				
Site A		103 ± 5	-93 ± 4	+38 ± 5	-24 ± 5
Site C′		43 ± 6	-15 ± 4	-36 ± 5	-19 ± 8
Apollo 12:					
ALSEP Site	3.2°S, 23.4°W	38 ± 2	-25.8 ± 1.0	+11.9 ± 0.9	-25.8 ± 0.4

FIGURE CAPTIONS

Fig. 1 Apollo magnetometer network on the lunar surface. Maximum remanent magnetic fields measured at each landing site are shown.

Fig. 2 Orbit of the moon projected onto the solar ecliptic plane. During a complete revolution around the earth, the moon passes through the earth's bow shock, the magnetosheath, the geomagnetic tail, and the interplanetary region dominated by solar plasma fields. The insert shows an orbit of the Explorer 35 spacecraft, also projected onto the solar ecliptic plane.

Fig. 3 Apollo 16 magnetometers deployed on the moon at the Descartes landing site. (a) Lunar surface magnetometer (LSM). Sensors are at the top ends of the booms, approximately 75 cm above the lunar surface. (b) Lunar portable magnetometer (LPM), deployed during a magnetic field measurement by astronaut Young.

Fig. 4 Pictorial representation of the magnetic field vectors measured at the Apollo 16 Descartes region. The maximum field measured anywhere on the moon to date is that at site 13: 327 γ.

Fig. 5 Compression of the Apollo 16 remanent field by the solar wind plasma. (a) Simultaneous plots of magnetic energy density and plasma bulk energy density. The magnetic energy density shown is computed from the difference between the compressed and uncompressed remanent field at the Apollo 16 site, i.e. $\Delta B^2 = \sum_i \left(B_{Ai} - (B_{Ei} + B_{Ri})\right)^2$, $i = x,y,z$. These field components and the ALSEP coordinate system (x,y,z) are defined in the text. Plasma energy density data are from the Apollo 15 solar wind spectrometer, courtesy of C.W. Snyder and D.R. Clay of the Jet Propulsion Laboratory; N is the proton number density, m is the proton mass, and v is the plasma bulk speed. (b) Schematic representation of remanent field compression by

a high-density solar wind plasma. The remanent field is unperturbed during nighttime (antisolar side), while on the sunlit side it is compressed.

Fig. 6 Magnetic energy density versus plasma energy density at two Apollo sites which have different remanent magnetic fields. Energies are defined in Fig. 5. Uncompressed remanent field magnitudes are 38 γ at Apollo 12 and 235 γ at Apollo 16. Apollo 12 magnetometer data are plotted versus Apollo 12 solar wind spectrometer (SWS) data, while Apollo 16 magnetometer data are plotted versus Apollo 15 SWS data. SWS data are courtesy of C.W. Snyder and D.R. Clay of the Jet Propulsion Laboratory.

Fig. 7 Eddy currents and corresponding poloidal magnetic field, induced by time-dependent fluctuations in the solar wind magnetic field $\underline{B}_E$. This global induced field is confined by the solar wind flowing past the moon; the field is compressed on the lunar sunlit side and confined in the cavity region on the nighttime (antisolar) side of the moon.

Fig. 8 Nighttime transient response magnetic field data. A transient measured by an Apollo LSM while on the nighttime (antisolar) side of the moon, showing simultaneous external solar wind field data measured by Explorer 35. The ALSEP (x,y,z) coordinate system is defined in the text.

Fig. 9 (a) Lunar electrical conductivity profile and

(b) temperature profile of the moon. Shown are previous profiles (Dyal and Parkin, 1973) using vacuum nightside theory and nightside magnetometer data. Superimposed on (a) is a conductivity profile calculated by fitting totally confined 2-layer moon models to the dayside tangential component data illustrated in Fig. 11.

Fig. 10 Daytime transient response magnetic field data, measured by an Apollo LSM while on the dayside (subsolar) side of the moon, showing simultaneous external solar wind field data measured by lunar orbiting Explorer 35.

The ALSEP (x,y,z) coordinate system is defined in the text. Note in particular the tangential components: dayside overshoot amplification is much higher relative to the Explorer-measured external step magnitudes than is nighttime amplification (shown in Fig. 8).

Fig. 11 Normalized daytime transient response data, showing decay characteristics of tangential components ($B_{Ay,z}$) of the total surface field after arrival of a step transient which changes the external magnetic field tangential component by an amount $\Delta B_{Ey,z}$, here normalized to one. The shape of the curve illustrates time-decay characteristics of the induced poloidal eddy current field $\underline{B}_P$. Superimposed are conductivity-dependent theoretical response curves for a totally confined moon.

Fig. 12 Confinement of a point dipole magnetic field. Shown are theoretical profiles and experimental data. The inserts schematically show lunar confinement by the solar wind, approximated by a capped-cylinder superconductor enclosing a point-dipole field. The theoretical curves show ratios of confined to unconfined dipolar field versus distance along the cylinder axis. Data are results of a laboratory experiment in which confinement of a small dipole magnet's field by a cylindrical superconductor is measured experimentally.

Fig. 13 Induced magnetization field $\underline{B}_\mu$. When a homogenous sphere of permeability $\mu > \mu_o$ is immersed in a uniform external magnetic field $\underline{B}_E$ (for example, the moon in the steady geomagnetic tail field), a dipolar magnetic field $\underline{B}_\mu$ is induced with its dipole moment aligned with $\underline{B}_E$. If the magnetizing field $\underline{B}_E$ and the magnetic induction ($\underline{B}_E + \underline{B}_\mu$) are known, a classical B-H hysteresis curve can be constructed from the data,

Fig. 14 Hysteresis curve of the moon. The moon is immersed in the steady external magnetizing geomagnetic tail field $\underline{B}_E$ (measured by Explorer 35); the total

magnetic induction is $\underline{B}_A = \underline{B}_E + \underline{B}_\mu$ measured by the Apollo 12 lunar surface magnetometer, where $\underline{B}_\mu$ the induced lunar magnetization field. In this graph only the radial (x) components are plotted. From the slope of the curve the bulk relative permeability is calculated: $\mu/\mu_o = 1.029\ ^{+0.024}_{-0.019}$.

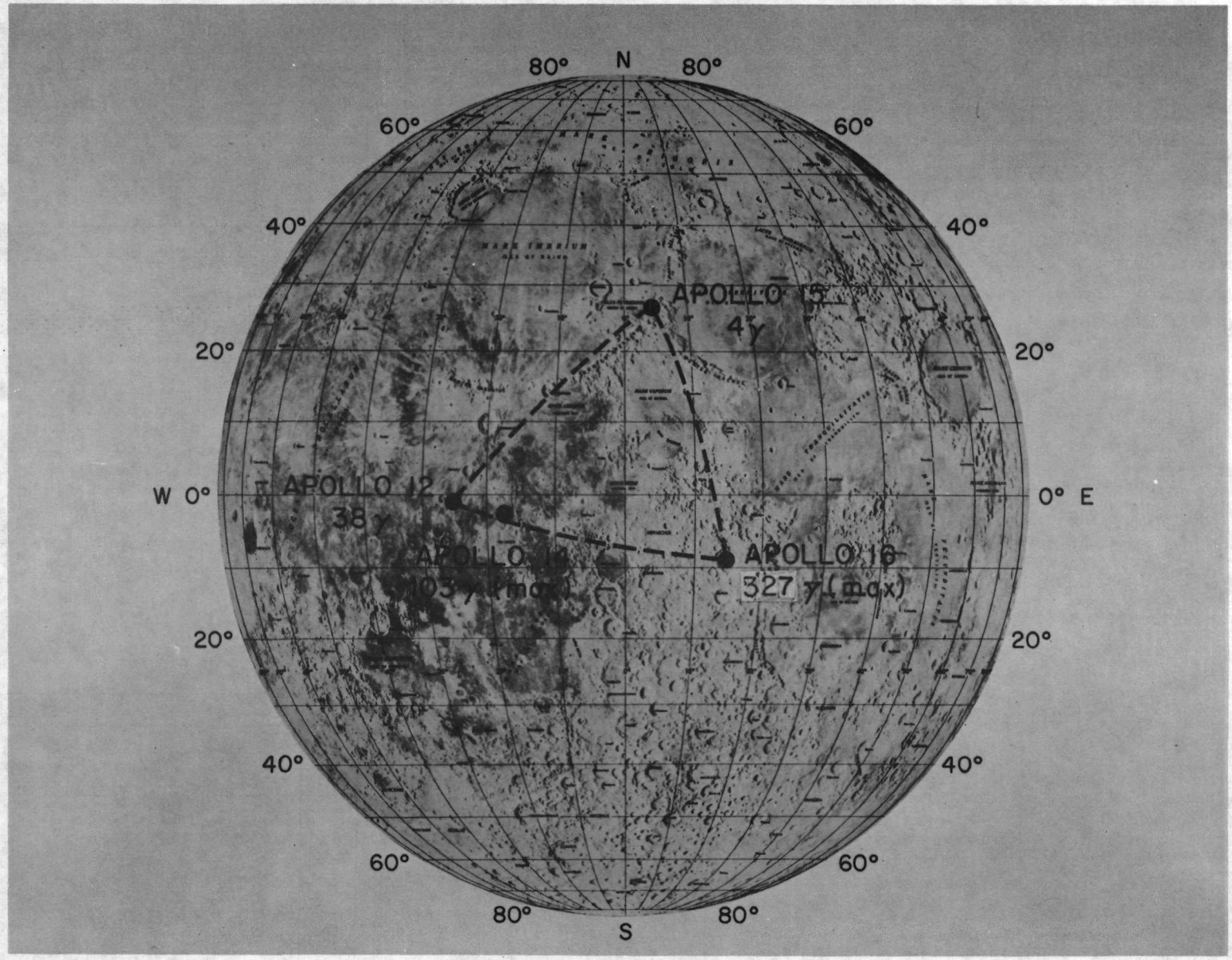
80° N 80°
60° 60°
40° 40°
20° 20°
W 0° 0° E
20° 20°
40° 40°
60° 60°
80° S 80°
APOLLO 15
4 γ
APOLLO 12
38 γ
APOLLO 16
327 γ (max)

Fig. 1

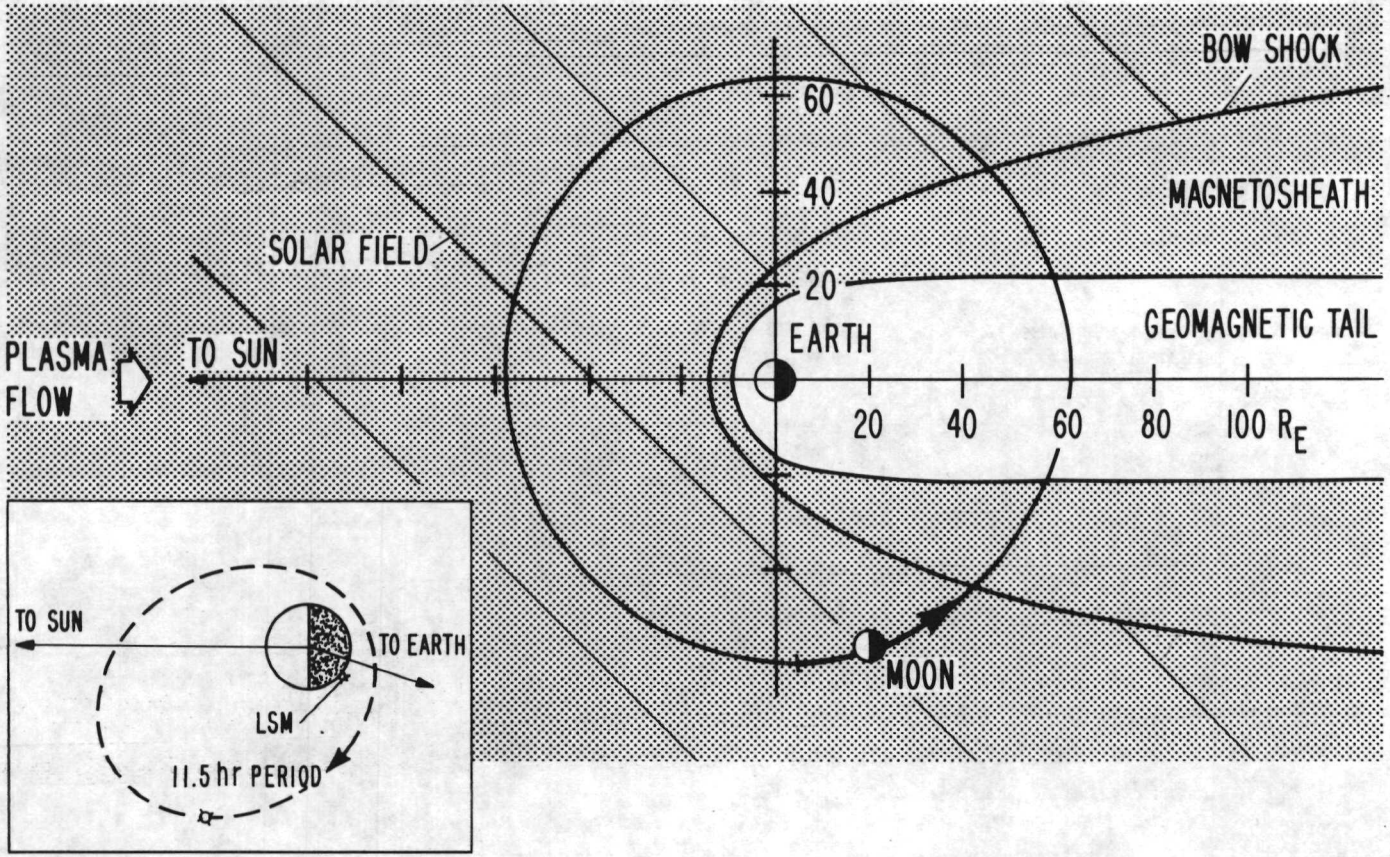
BOW SHOCK
60
40
MAGNETOSHEATH
SOLAR FIELD
20
EARTH
GEOMAGNETIC TAIL
PLASMA FLOW
TO SUN
20
40
60
80
100 R_E
TO SUN
TO EARTH
LSM
11.5 hr PERIOD
MOON

Fig. 2

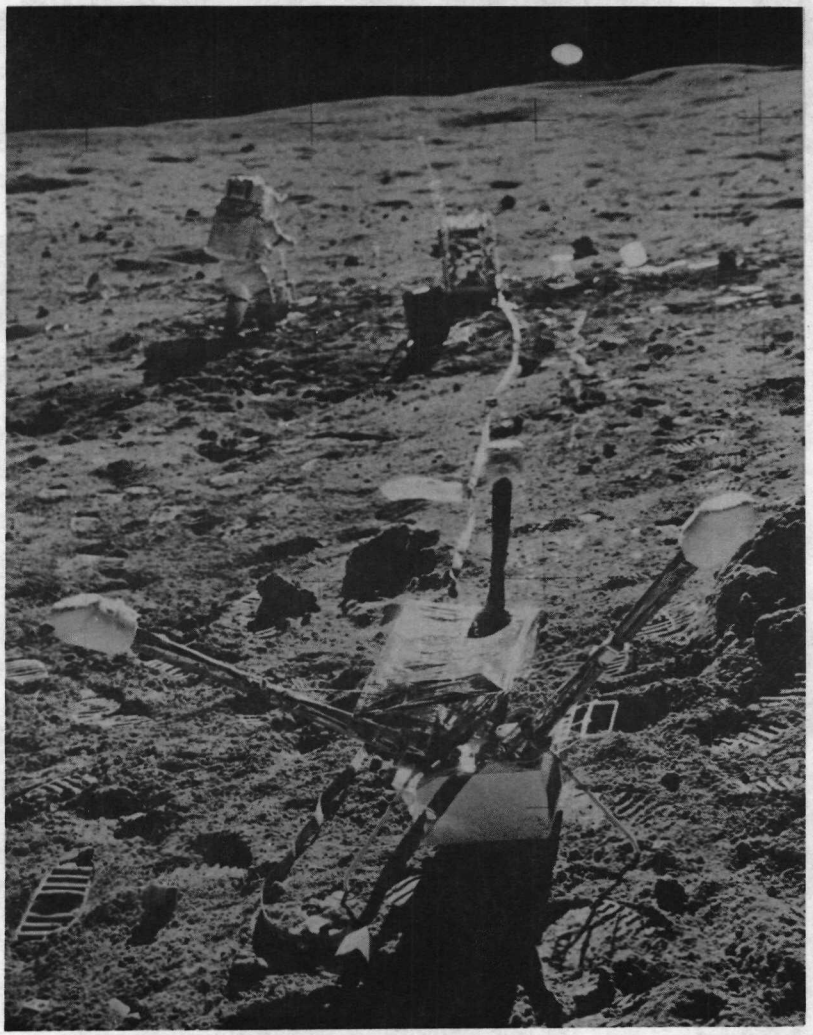

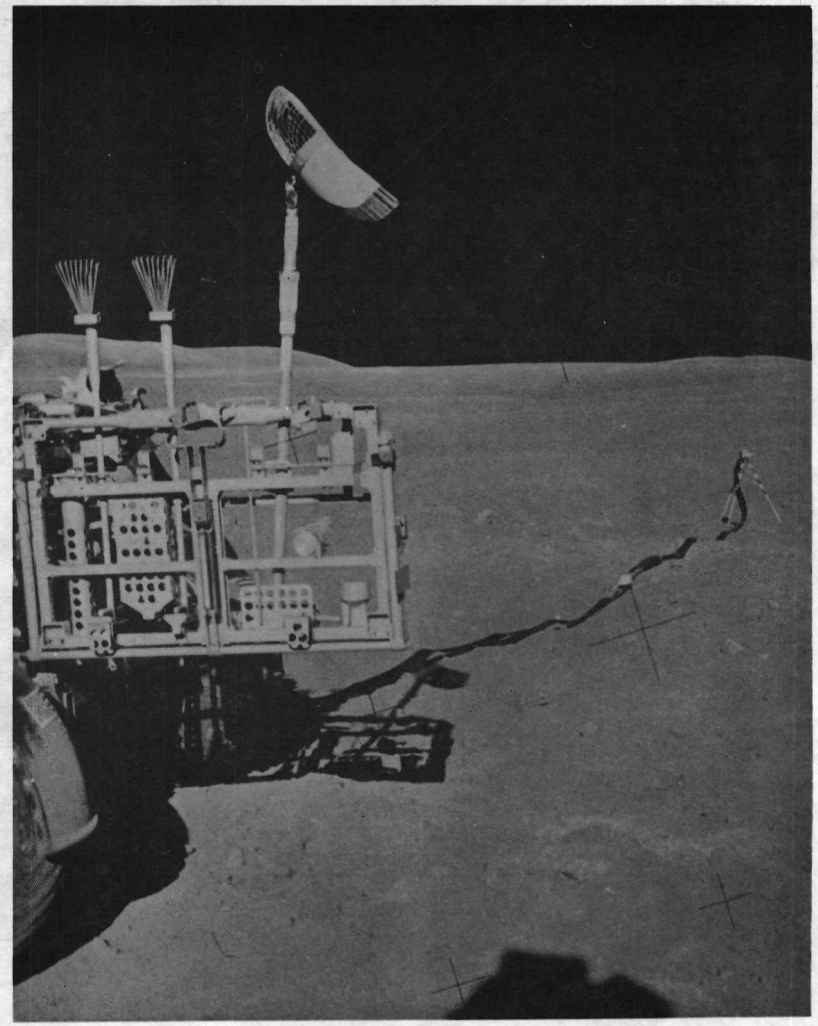

Fig. 3

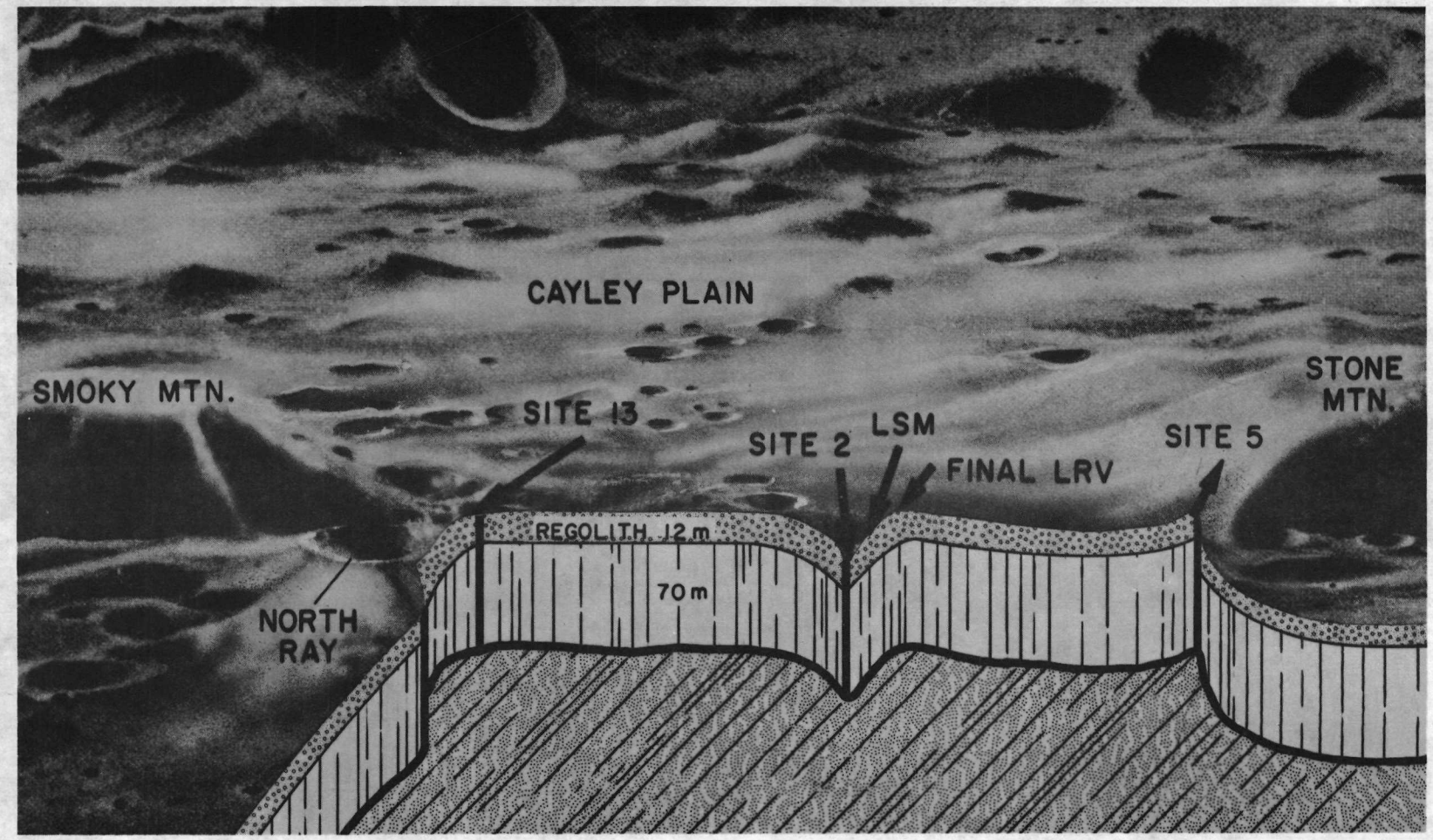
CAYLEY PLAIN
SMOKY MTN.
SITE 13
SITE 2
LSM
FINAL LRV
SITE 5
STONE MTN.
REGOLITH 12 m
70 m
NORTH RAY

Fig. 4

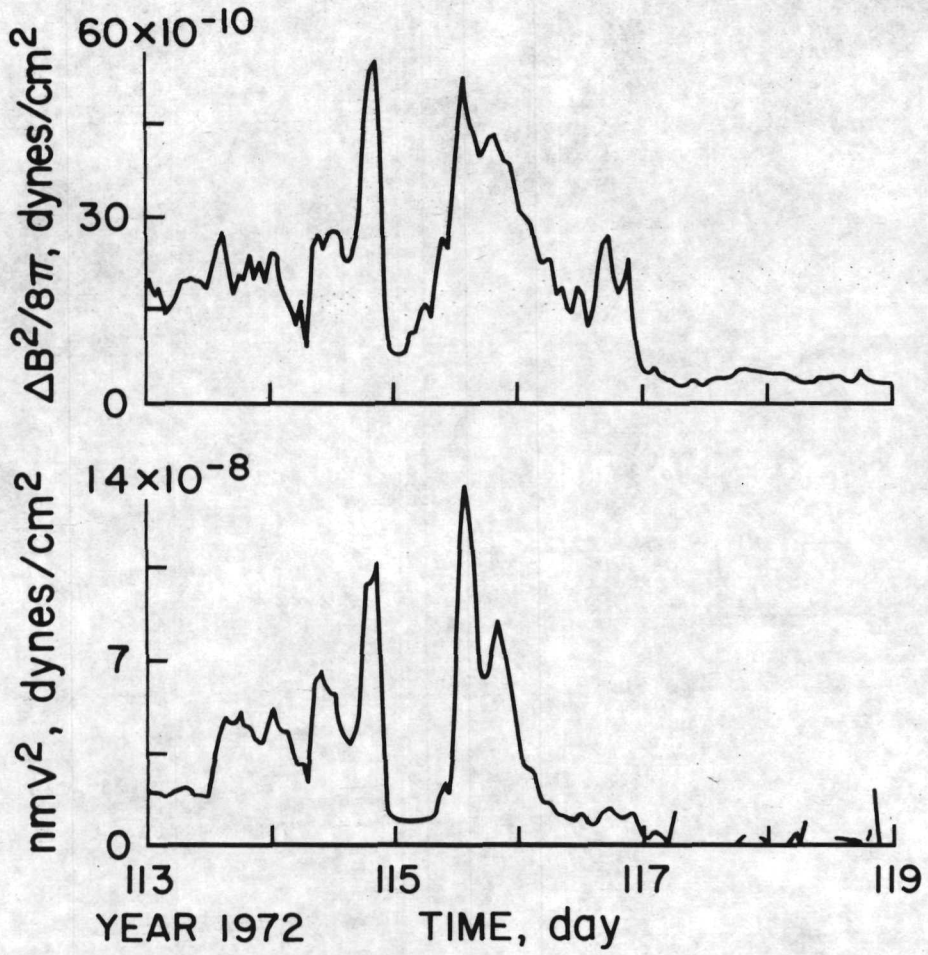
60×10⁻¹⁰
30
0
ΔB²/8π, dynes/cm²
14×10⁻⁸
7
0
nmV², dynes/cm²
113
115
117
119
YEAR 1972
TIME, day

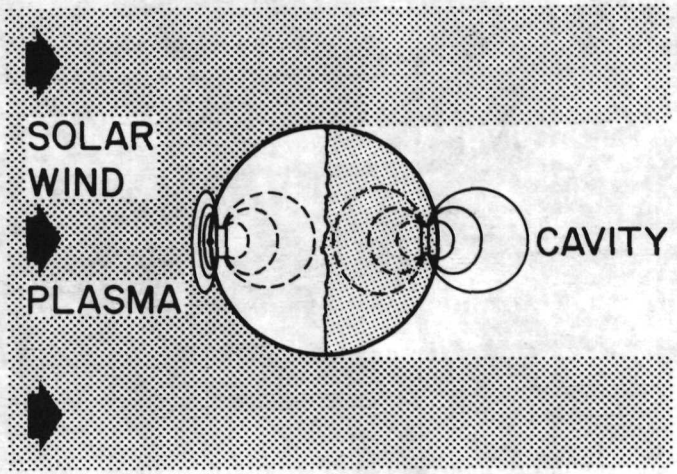
SOLAR
WIND
PLASMA
CAVITY

Fig. 5

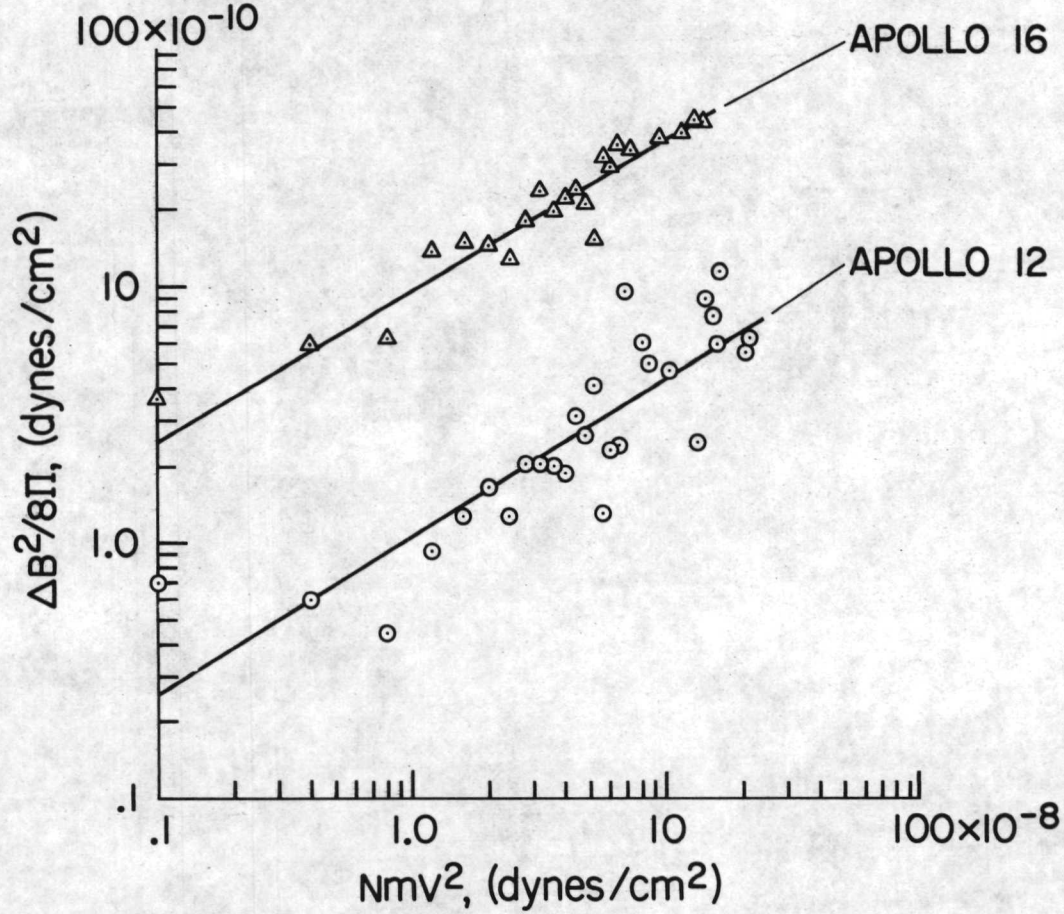
100×10⁻¹⁰
10
1.0
.1
ΔB²/8Π, (dynes/cm²)
APOLLO 16
APOLLO 12
.1
1.0
10
100×10⁻⁸
Nmv², (dynes/cm²)

Fig. 6

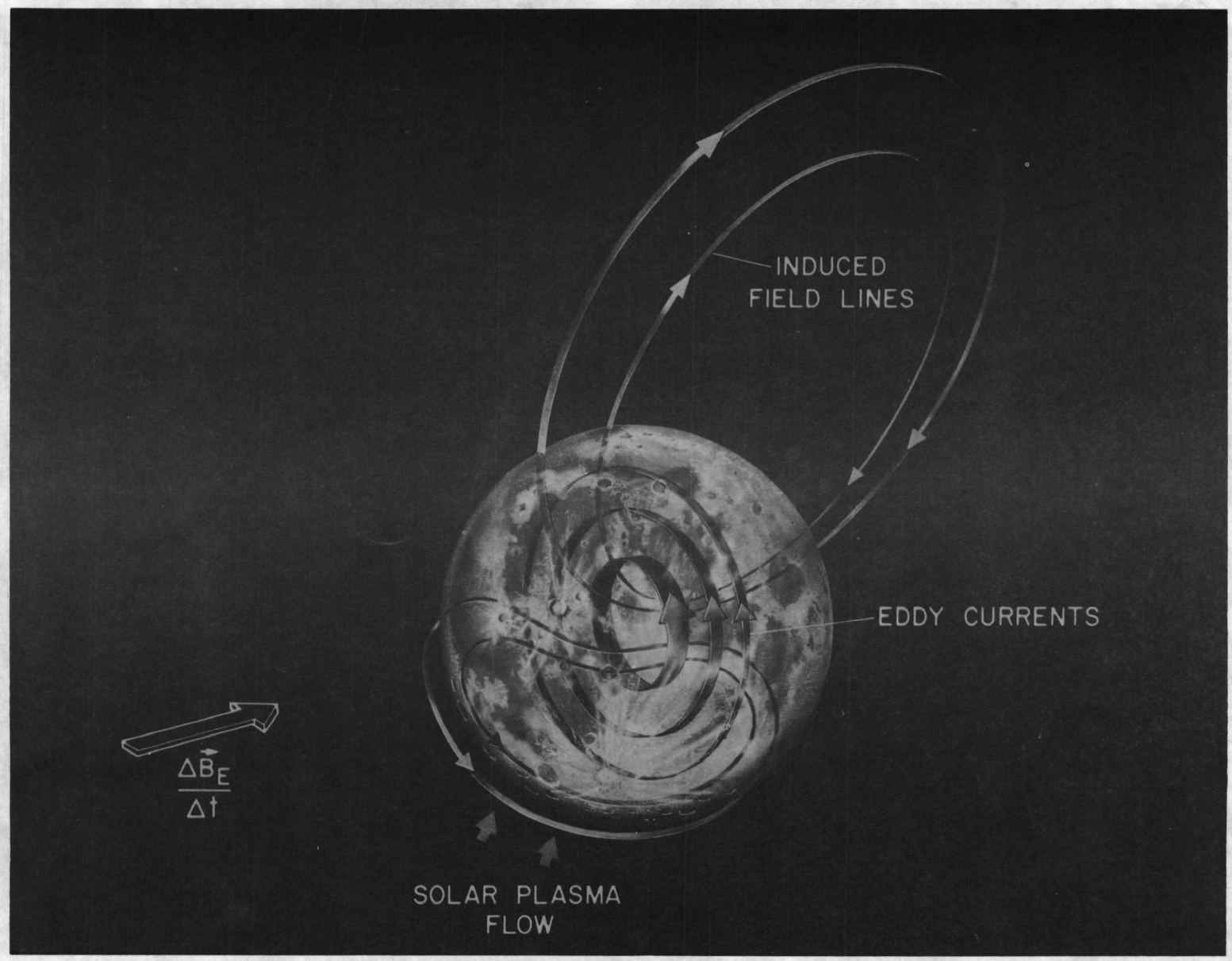
INDUCED
FIELD LINES
EDDY CURRENTS
$\frac{\Delta \vec{B}_E}{\Delta t}$
SOLAR PLASMA
FLOW

Fig. 7

NIGHTTIME TRANSIENT RESPONSE

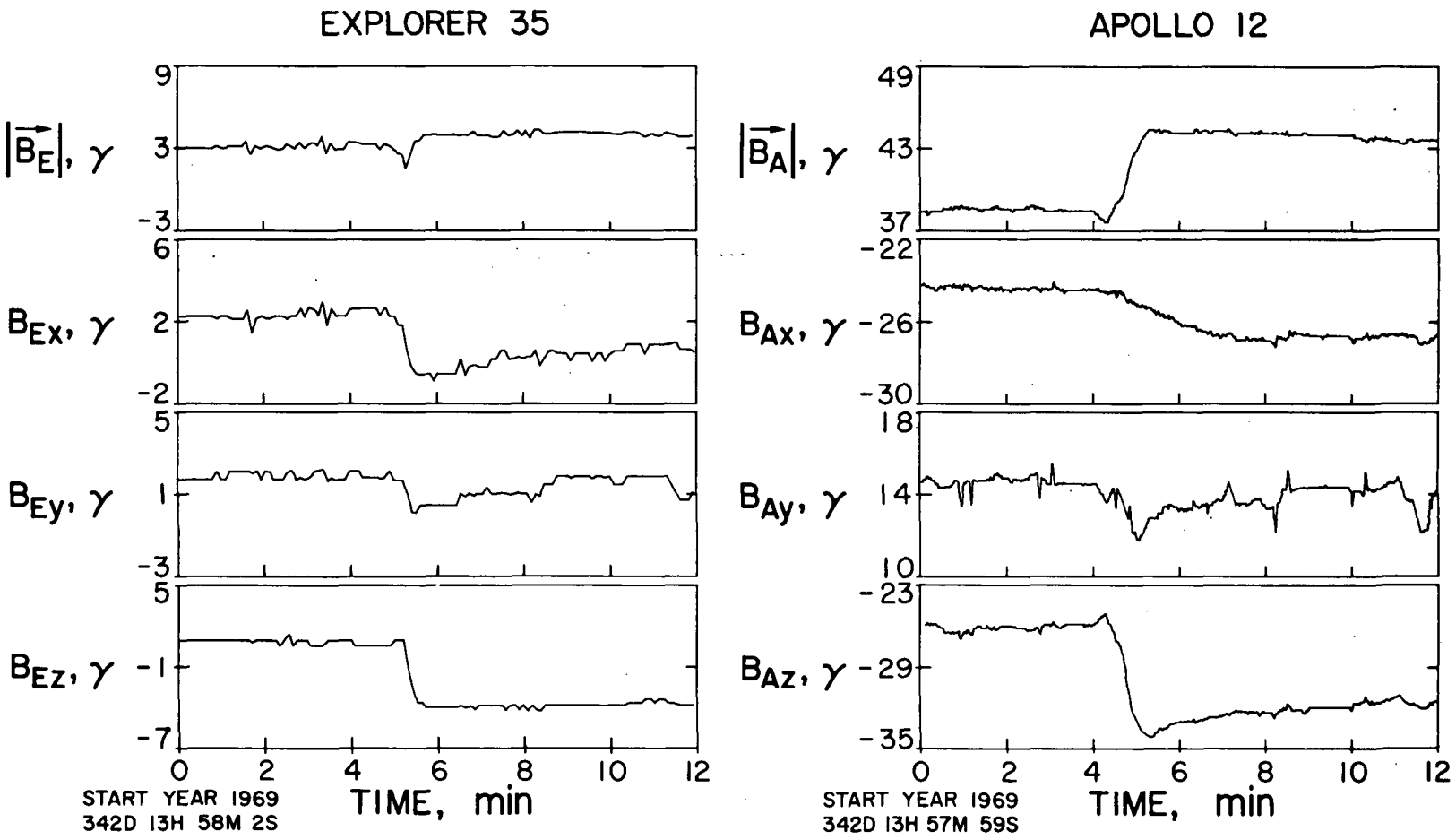

Fig. 8

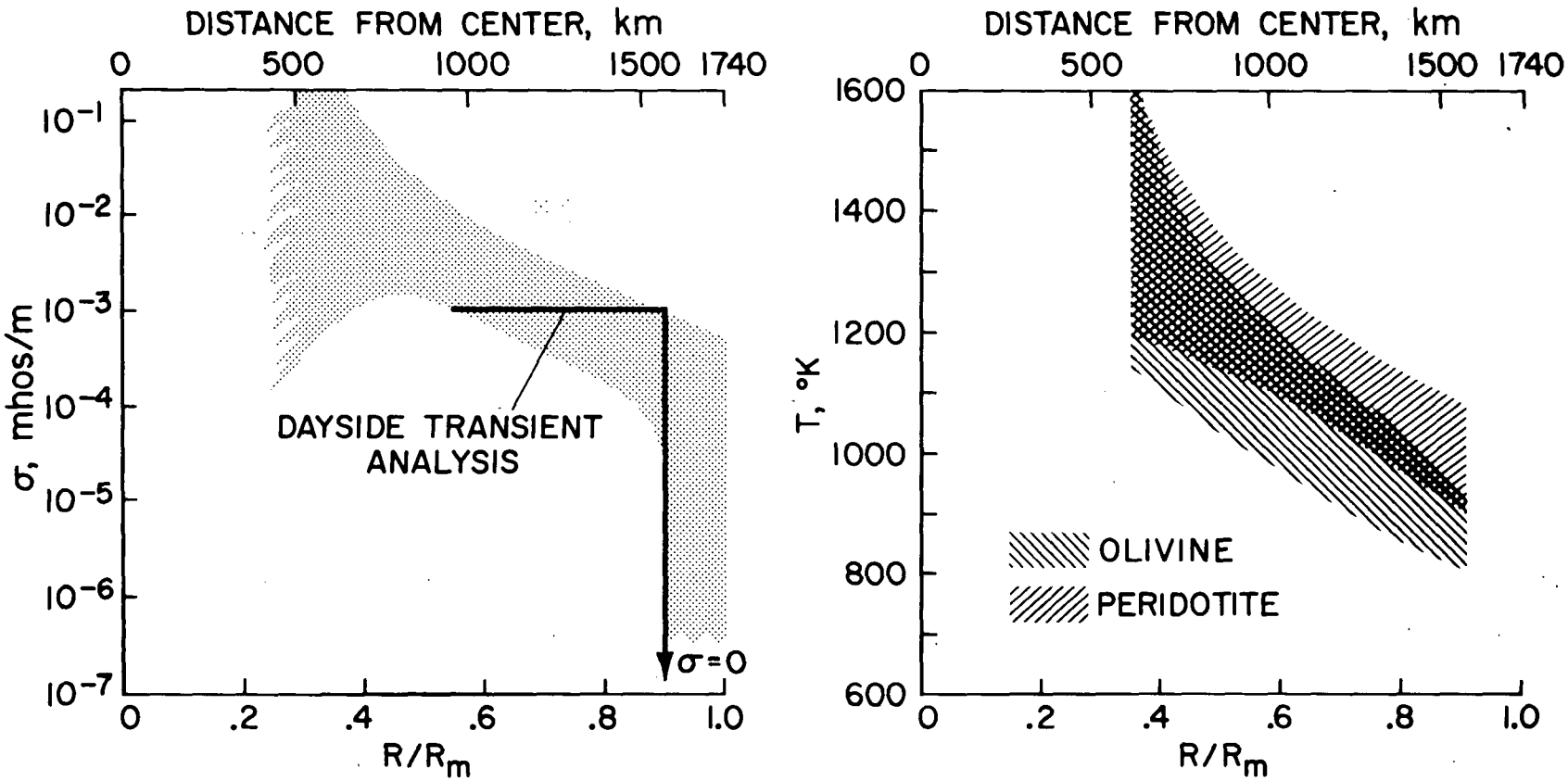
DISTANCE FROM CENTER, km
0
500
1000
1500
1740
10^{-1}
10^{-2}
10^{-3}
10^{-4}
10^{-5}
10^{-6}
10^{-7}
σ, mhos/m
DAYSIDE TRANSIENT ANALYSIS
σ=0
0
.2
.4
.6
.8
1.0
R/Rm
DISTANCE FROM CENTER, km
0
500
1000
1500
1740
1600
1400
1200
1000
800
600
T, °K
OLIVINE
PERIDOTITE
0
.2
.4
.6
.8
1.0
R/Rm

Fig. 9

DAYTIME TRANSIENT RESPONSE

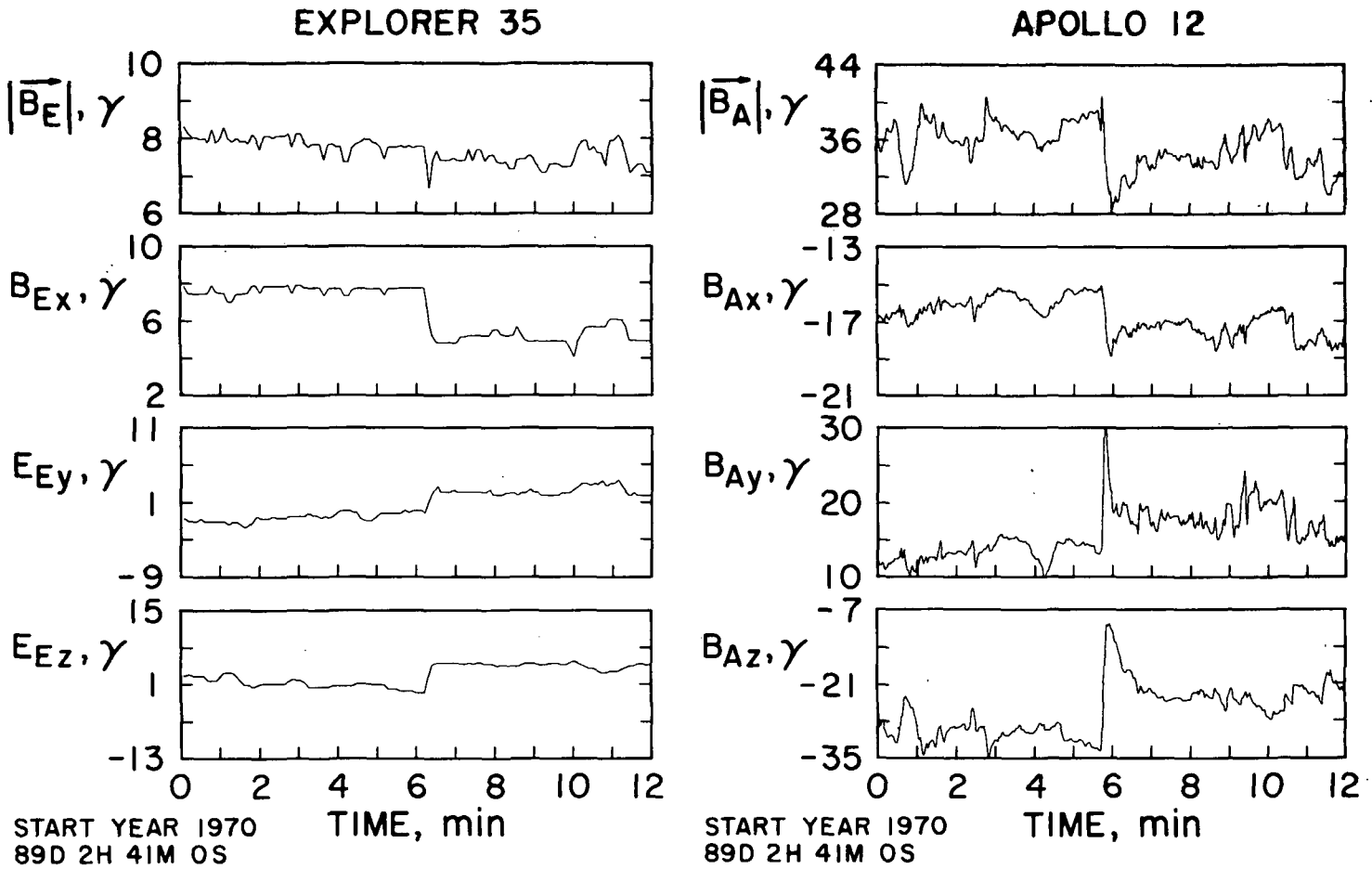

Fig. 10

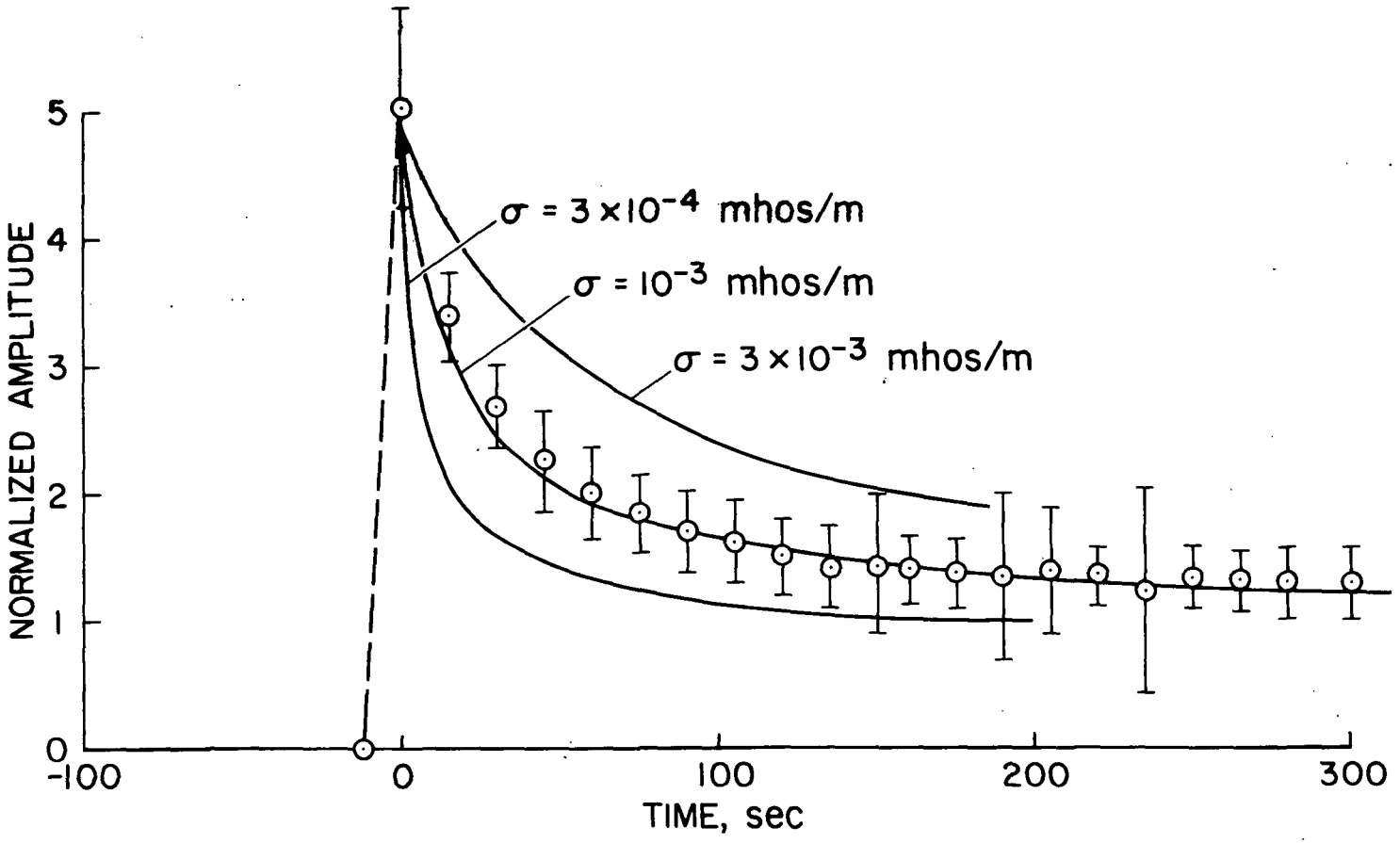
NORMALIZED AMPLITUDE
5
4
3
2
1
0
-100
0
100
200
300
TIME, sec
σ = 3×10⁻⁴ mhos/m
σ = 10⁻³ mhos/m
σ = 3×10⁻³ mhos/m

Fig. 11

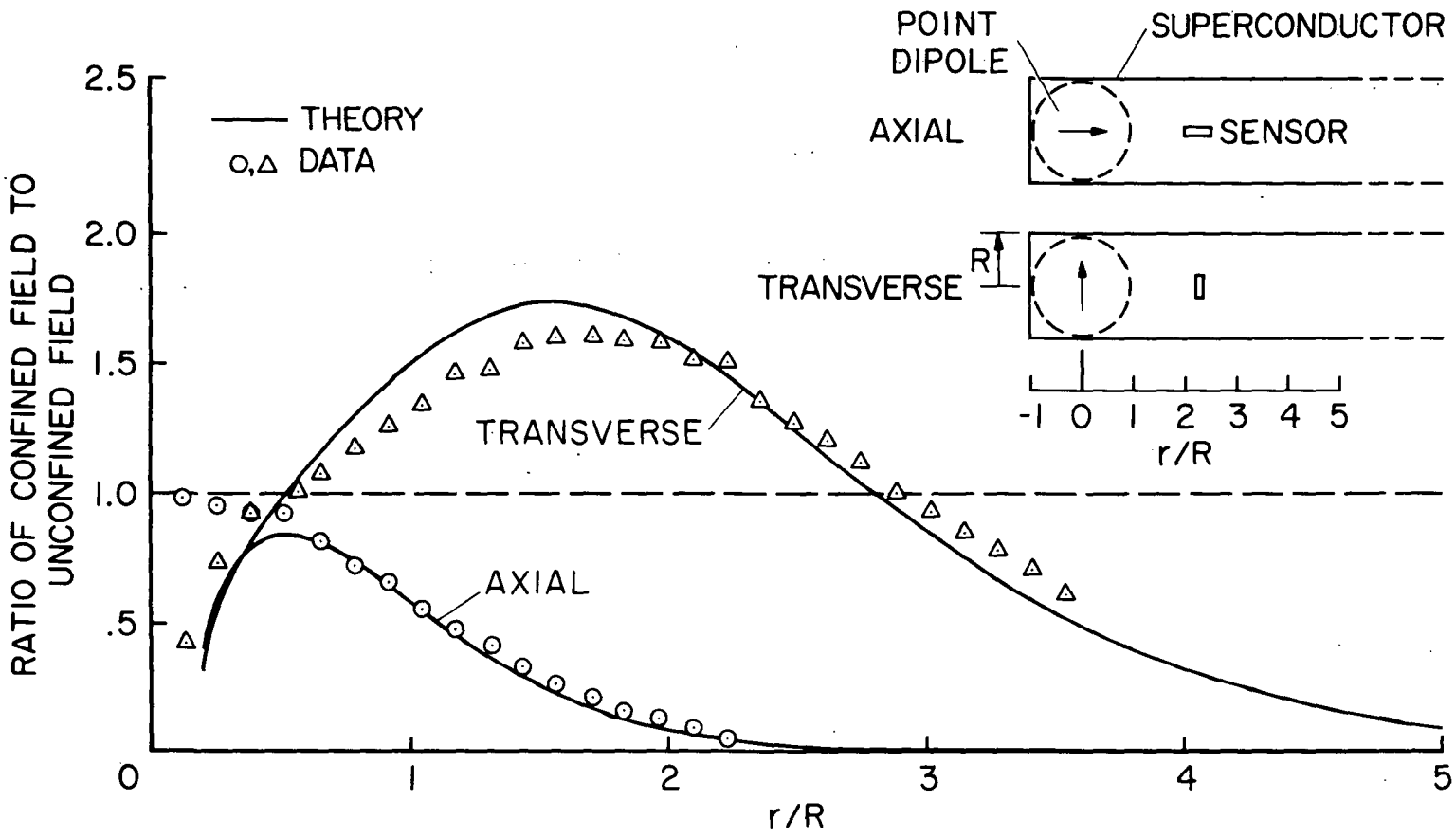
POINT DIPOLE
SUPERCONDUCTOR
AXIAL
SENSOR
TRANSVERSE
R
-1 0 1 2 3 4 5
r/R
THEORY
o,Δ DATA
RATIO OF CONFINED FIELD TO UNCONFINED FIELD
2.5
2.0
1.5
1.0
.5
TRANSVERSE
AXIAL
0 1 2 3 4 5
r/R

Fig. 12

EXTERNAL (TERRESTRIAL) FIELD $\vec{B}_E$

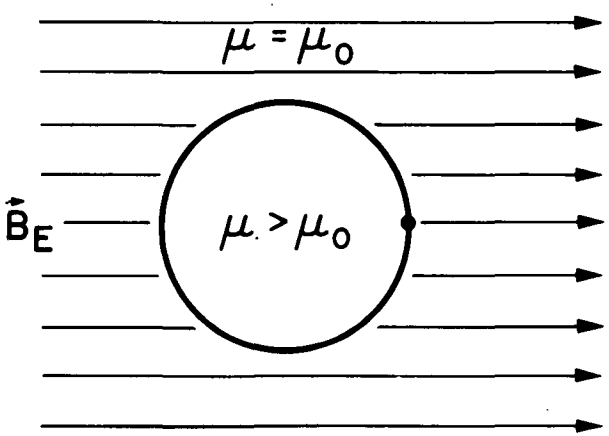

INDUCED MAGNETIZATION FIELD $\vec{B}_\mu$

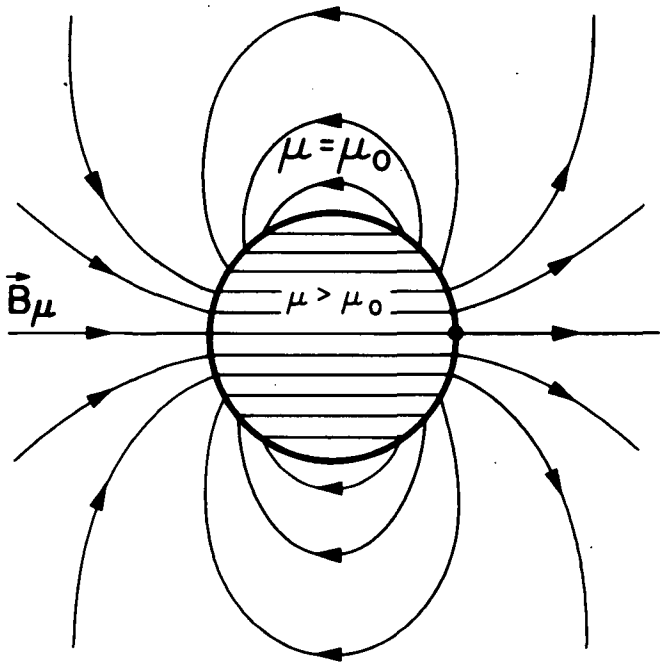

$$\vec{B}_A = \vec{B}_E + \vec{B}_\mu$$

Fig. 13

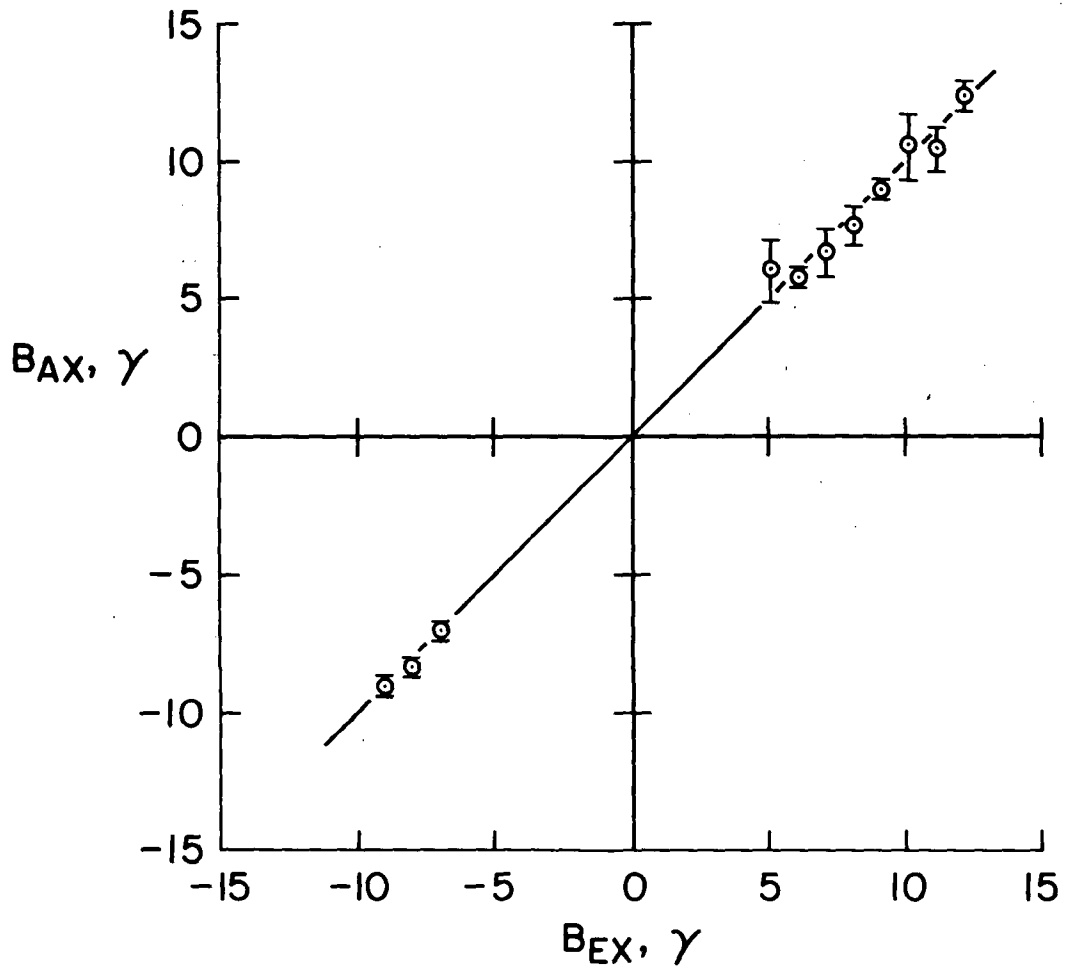

Fig. 14